Unmasking Steps in Intramolecular Aromatic Hydroxylation by a Synthetic Nonheme Oxoiron(IV) Complex
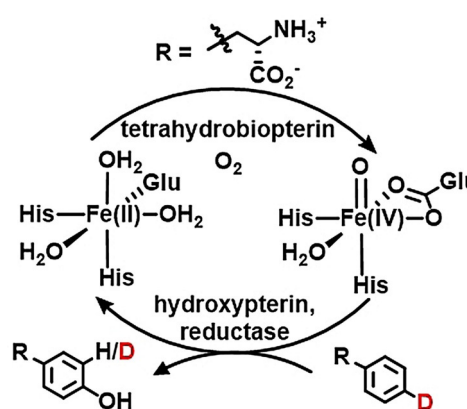
Yuan Sheng, Chase S. Abelson, Jai Prakash, Apparao Draksharapu, Victor G. Young, Jr., and Lawrence Que, Jr.*

*Abstract: In this study, a methyl group on the classic tetramethylcyclam (TMC) ligand framework is replaced with a benzylic group to form the metastable $[Fe^{IV}(O_{syn})\text{-}(Bn3MC)]^{2+}$ (**2-syn**; Bn3MC = 1-benzyl-4,8,11-trimethyl-1,4,8,11-tetraazacyclotetradecane) species at −40°C. The decay of **2-syn** with time at 25°C allows the unprecedented monitoring of the steps involved in the intramolecular hydroxylation of the ligand phenyl ring to form the major Fe^{III}−OAr product **3**. At the same time, the $Fe^{III}(Bn3MC)^{2+}$ (**1**) precursor to **2-syn** is re-generated in a 1:2 molar ratio relative to **3**, accounting for the first time for all the electrons involved and all the Fe species derived from **2-syn** as shown in the following balanced equation: $3[Fe^{IV}(O)(L^{Ph})]^{2+}$ (**2-syn**)→ $2[Fe^{III}(L^{OAr})]^{2+}$ (**3**) + $[Fe^{II}(L^{Ph})]^{2+}$ (**1**) + H_2O. This system thus serves as a paradigm for aryl hydroxylation by Fe^{IV}=O oxidants described thus far. It is also observed that **2-syn** can be intercepted by certain hydrocarbon substrates, thereby providing a means to assess the relative energetics of aliphatic and aromatic C−H hydroxylation in this system.*

Introduction

The direct functionalization of aromatic rings is by nature of interest to researchers.[1] Owing to the high stability of aromatic rings, these synthetic methods are mostly found to require either harsh acidic conditions or catalysis by late transition metals.[2] Nature provides us the inspiration by utilizing the combination of iron and oxygen atoms to generate a highly reactive oxoiron(IV) (Fe^{IV}=O) species that is capable of selectively hydroxylating the arene-containing amino acids within an acid-sensitive protein framework.[3] Phenylalanine hydroxylase (PheH), tyrosine hydroxylase (TyrH), and tryptophan hydroxylase (TrpH) make up this small family of pterin-dependent nonheme iron enzymes,[3] all of which play pivotal roles in important biological transformations. PheH controls the level of phenylalanine by converting it to tyrosine, while its malfunction is associated with a severe metabolic disorder called phenylketonuria. TyrH and TrpH are responsible for the respective biosynthesis

of the key precursors to dopamine and serotonin, neurotransmitters that affect our mood and behavior. These enzymes utilize the combination of dioxygen and a tetrahydrobiopterin cofactor to generate Fe^{IV}=O species from their Fe^{II} resting states,[3] as evidenced directly by Mössbauer spectroscopy,[4] to incorporate an oxygen atom onto their namesake amino acids (Scheme 1).

Scheme 1. General mechanism proposed for pterin-dependent hydroxylases with phenylalanine hydroxylase shown as an example.

On the other hand, the properties of nonheme Fe^{IV}=O species have been broadly investigated since the report of the first crystal structure of a synthetic Fe^{IV}=O complex in 2003 by Que, Nam and co-workers.[5] Such synthetic Fe^{IV}=O complexes have significantly increased in number over the past twenty years and exhibit different lifetimes and a range of reactivity properties.[6]

Most of these complexes possess iron(IV) centers with an intermediate spin state ($S = 1$),[6] in contrast to the more reactive high-spin ($S = 2$) species found in the enzymes.[7] The best documented reactions performed by synthetic Fe^{IV}=O species are hydrogen atom transfer (HAT) reactions,[6] in which the Fe^{IV}=O species abstracts an H atom from a substrate C−H bond, generating a meta-stable Fe^{III}−OH species and an organic radical that can in principle combine to form the product C−OH bond by oxygen rebound. However, this step is often not fast enough, thus allowing the substrate radical to escape from the solvent cage and be intercepted by O_2.[8]

To date, the reactivity of synthetic Fe^{IV}=O species with respect to two-electron transfer has mainly been exemplified by oxygen atom transfer (OAT) reactions to phosphines or

[*] Y. Sheng, C. S. Abelson, Dr. J. Prakash, Dr. A. Draksharapu,
Dr. V. G. Young Jr., Prof. Dr. L. Que, Jr.
Department of Chemistry, University of Minnesota
Minneapolis, MN 55455 (USA)
E-mail: larryque@umn.edu

Angew. Chem. Int. Ed. **2021**, *60*, 20991–20998

© 2021 Wiley-VCH GmbH
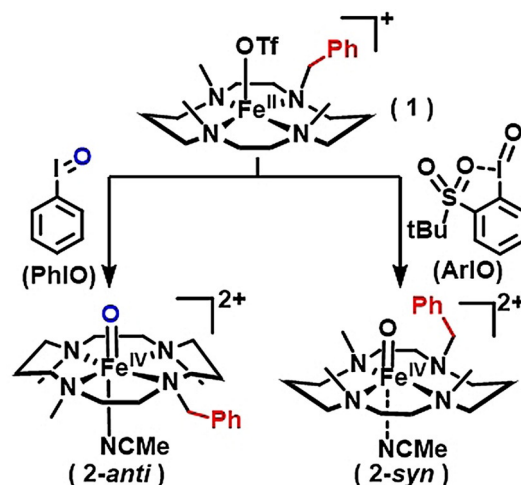
Wiley Online Library 20991

thioethers, which are substrates that readily form corresponding oxides. Much less common are examples of more intriguing reactions such as olefin epoxidation,[9] where the O atom is transferred to a C=C bond, or aromatic hydroxylation, where O atom transfer results in the functionalization of the aromatic ring.[10] With respect to the latter, no $Fe^{IV}=O$ species characterized to date has been reported to convert benzene directly to phenol. The most closely related reaction analogue is the oxidation of anthracene to anthraquinone investigated by Nam and de Visser.[10a] More success has been achieved in the hydroxylation of phenyl rings that are incorporated into the supporting ligand framework to place them in close proximity to the $Fe^{IV}=O$ units.[10b–d,11] However, it has been challenging to trap and characterize the $Fe^{IV}=O$ oxidant prior to its reaction with its pendant phenyl group.

In fact, only in this past decade has direct evidence been found for $Fe^{IV}=O$ species that hydroxylate a phenyl ring built into the supporting ligand framework to generate an Fe^{III}–OAr product. Using a C_3-symmetric tripodal ligand with pendant phenyl rings, Chang reported the trapping of an $Fe^{IV}=O$ complex at −40°C that upon warming underwent intramolecular conversion into an Fe^{III}–OAr species.[10b] Subsequently, Goldberg and co-workers introduced fluorine atoms to block the 2,6-positions of the phenyl groups on a phenyl-modified N4Py ligand (N4Py = N,N-bis(2-pyridylmethyl)bis(2-pyridyl)methylamine) to trap an $Fe^{IV}=O$ complex, which was characterized at −20°C with cold-spray ionization mass spectrometry (CSI-MS) and Mössbauer spectroscopy.[10c] Warming to ambient temperature led to the unprecedented cleavage of the aromatic C−F bond to generate the Fe^{III}–OAr product. A subsequent study showed that complexes with MeO-substituted phenyl groups on the ligand accelerated the aryl hydroxylation rate, strongly implicating the involvement of an electrophilic transition state that generated chromophoric Fe^{III}–OAr products.[10c,d]

The observation of such Fe^{III}–OAr products in the synthetic reactions instead of $Fe^{II}(L^{Ar–OH})$ species suggests that there is a facile subsequent one-electron oxidation step that prevents the reaction from becoming catalytic, unlike in the case of phenylalanine hydroxylase, in which the tyrosine product dissociates to allow the iron center to be primed for the next cycle of substrate oxidation. To date, however, the mechanistic details for hydroxylating a pendant aromatic group have not been sufficiently uncovered to provide useful mechanistic insight into how to unleash the potential of $Fe^{IV}=O$ species for effecting aromatic hydroxylation reactions. We describe our efforts below.

Results and Discussion

Our efforts start with Bn3MC (1-benzyl-4,8,11-trimethyl-1,4,8,11-tetraaza-cyclotetradecane), a variant of the widely studied macrocyclic TMC ligand framework (TMC = 1,4,8,11-tetramethyl-1,4,8,11-tetraazacyclotetradecane), which is known for its ability to support a relatively stable $Fe^{IV}=O$ unit with a $t_{1/2}$ of 10 h at 25°C.[5] In this structure, the oxo atom is bound to the iron center on the face opposite to all four methyl groups of the TMC ligand (Scheme 2). Subsequent

Scheme 2. Generation of the *anti* (**2-anti**) and *syn* (**2-syn**) isomers of $[Fe^{IV}(O)(Bn3MC)]^{2+}$ from $Fe^{II}(Bn3MC)(OTf)^+$ (**1**) with the respective use of PhIO and 2-(t-BuSO$_2$)C$_6$H$_4$IO (s-ArIO) as oxo-transfer reagents in MeCN. Benzyl groups are marked in red for emphasis.

studies have led to the characterization of the isomeric $[Fe^{IV}(O_{syn})(TMC)(NCMe)](OTf)_2$ in which the oxo moiety is positioned on the same face as all four methyl groups.[12] It is thus anticipated that the corresponding isomers with the Bn3MC ligand can be generated (Scheme 2), with the benzyl group on the *syn* isomer expected to be in the correct orientation for hydroxylation by the $Fe^{IV}=O$ unit. In fact, the results of this investigation confirm this hypothesis.

The detailed characterization of $[Fe^{II}(Bn3MC)(OTf)]$-(OTf) (**1**) is described in the SI. Its crystal structure (Figure S15) shows the expected arrangement of ligating N atoms from the macrocyclic ligand and an axial triflate. Its ^1H NMR spectrum (Figure 1) reveals features similar to those of $Fe^{II}(TMC)(OTf)_2$ but is more complex due to the loss of C_{2v} symmetry upon the replacement of one of the four methyl
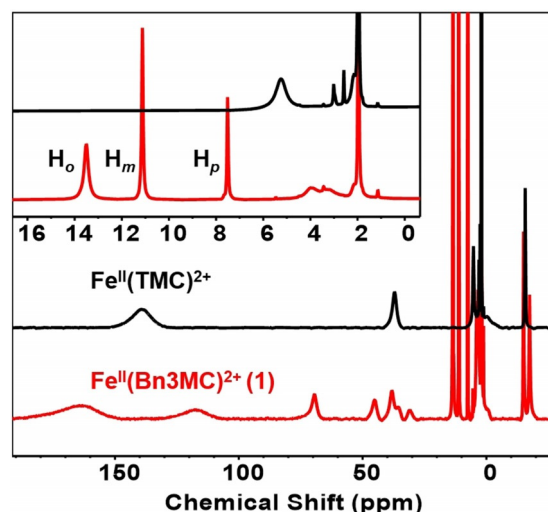

Figure 1. ^1H NMR spectra of **1** (red trace) and the TMC analogue (black trace) in MeCN-d_3 at 298 K. Inset shows the 0–16 ppm region where the sharp phenyl proton signals on **1** can be found.

groups with a benzyl group. The remaining three methyl groups are found at 163 and 117 ppm with an approximate 2:1 intensity ratio. These peaks exhibit a weighted average chemical shift of 148 ppm, close to that of the 140 ppm peak assigned to its four methyl groups in $Fe^{II}(TMC)(OTf)_2$.[12]

The features arising from the benzyl substituent can be assigned to new peaks at 70 ppm and in the 7–14 ppm range. The 70 ppm peak has a linewidth comparable to those of a cluster of peaks around the 40 ppm region that are associated with CH_2 protons next to the N atoms of the macrocycle and has an integration of 2 H versus 8 H for the peak cluster at 40 ppm. The 70 ppm peak can thus be assigned to the methylene protons of the benzyl group. On the other hand, the three sharper peaks within the 7–14 ppm range with relative integrations of 2:2:1 from left to right can be associated with the ring protons of the benzyl group introduced in **1**. The broader peak at approximately 14 ppm is assigned to the much closer *ortho* protons (H_o), while the two sharper peaks can be associated with the *meta* (H_m) and *para* (H_p) protons from left to right based on their relative integrations and their narrower linewidths that reflect their greater distance from the iron center.

Generation of $[Fe^{IV}(O_{anti})(Bn3MC)]^{2+}$ (2-anti) and $[Fe^{IV}(O_{syn})(Bn3MC)]^{2+}$ (2-syn)

Based on previous work on the TMC-supported $Fe^{IV}=O$ species,[5,12] it is known that treating $Fe^{II}(TMC)(OTf)_2$ with different oxidants, specifically iodosylbenzene (PhIO) and 2-(*tert*-butylsulfonyl)iodosylbenzene (*s*-ArIO), results in the generation of distinct $Fe^{IV}=O$ species, even though their UV/Vis-NIR features look very similar. We have verified that parallel outcomes are obtained for the benzyl-substituted complex **1**. Thus, the reaction of **1** in MeCN with 1 equiv PhIO (dissolved in CF_3CH_2OH) at 233 K generates **2-anti** in quantitative yield with the appearance of its characteristic near-IR band at 831 nm ($\varepsilon_M = 400$, Figure 2, top panel). ESI-MS characterization of this new species shows a major peak at $m/z = 553.2$, indicating O atom incorporation into **1**, while its Raman spectrum exhibits a $\nu(Fe=O)$ at 842 cm^{-1} (Figure S2), similar to the 839 cm^{-1} peak found for $[Fe^{IV}(O_{anti})(TMC)-(NCMe)]^{2+}$.[13] The ^1H NMR spectrum of **2-anti**, compared to that of the corresponding TMC complex in Figure S3, shows similar features but is more complex due to the lower symmetry of the former. Warming this solution to 298 K over 60 min results in the loss of only 10% of the $Fe^{IV}=O$ complex, indicating its relative thermal stability (Figure 2, top panel).

In contrast, treating the same MeCN solution of **1** with 1.1 equiv *s*-ArIO (90% pure dissolved in a small amount of CD_2Cl_2) at 233 K results in the formation of a species with a similar near-IR band at 826 nm ($\varepsilon_M = 400$, Figure 2, bottom panel) but showing a distinct Fe=O Raman vibration at 860 cm^{-1} (Figure S2), which resembles the 858 cm^{-1} value associated with the $\nu(Fe=O)$ of $[Fe^{IV}(O_{syn})(TMC)-(NCMe)]^{2+}$.[13] This species is thus assigned to **2-syn**. The Raman spectrum of the **2-syn** sample also shows the presence of some **2-anti**, with relative intensities indicating a 4:1 **2-syn**/**2-anti** ratio. This observation is corroborated by the NMR
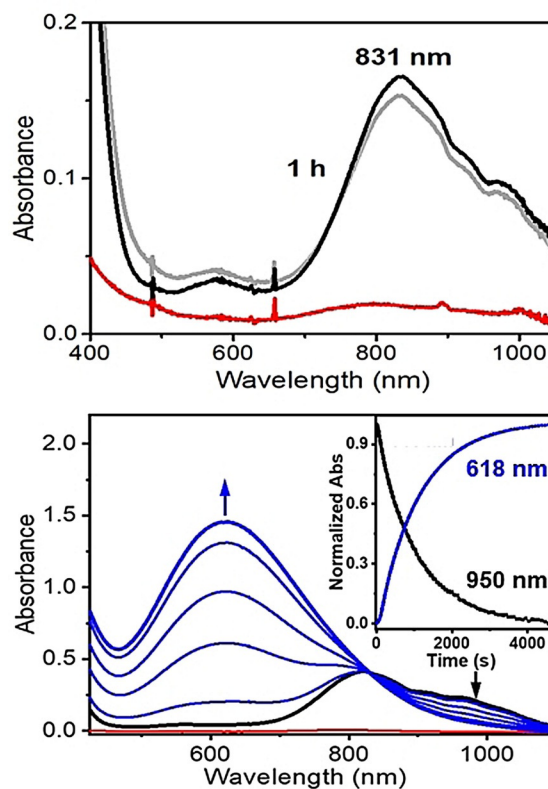

Figure 2. Top: Generation of **2-anti** (black trace) from a 0.45 mM solution of **1** (red trace) in MeCN at 298 K, gray trace represents the spectrum after standing for 1 h at 298 K. Bottom: Generation of **2-syn** (black trace) from a 1 mM solution of **1** (red trace) in MeCN at 298 K; the blue traces represent the generation of the product **3** over a 90 min period. Inset shows that the decrease of the absorbance at 950 nm following the decay of **2-syn** appears to be concomitant with the generation of **3** as indicated by the increase in the absorbance at 618 nm. The absorbances at 618 and 950 nm were normalized for the plot to emphasize that these steps appear to be governed by the same rate constant.

spectrum of this sample, which exhibits resonances for both **2-syn** and **2-anti** in a 4:1 intensity ratio (Figure S4), as previously observed in the reaction of $Fe^{II}(TMC)(OTf)_2$ with *s*-ArIO.[12] EXAFS analysis of a frozen MeCN solution of **2-syn** (Figure S16 and Table S1) reveals a first coordination sphere consisting of 1 O atom at 1.62 Å and 5 N/O atoms averaging 2.07 Å, in agreement with values found in the crystal structure of $[Fe^{IV}(O_{syn})(TMC)(OTf)]^+$ (Table S2).[13]

Conversion of $[Fe^{IV}(O_{syn})(Bn3MC)]^{2+}$ (2-syn) into 3 at 298 K

The thermal stability of **2-syn** significantly differs from that of the more stable **2-anti**. Unlike the latter, **2-syn** decays rapidly upon warming from 233 to 298 K, generating a blue species with an intense band centered at 618 nm (Figure 2, bottom) that is often associated with $Fe^{III}-OAr$ complexes.[14] This notion is confirmed by ESI-MS data that show a major peak at $m/z = 552.1$ with an isotope pattern associated with the $[Fe^{III}(Bn3MC)(OTf) + O - H]^+$ (**3**) ion, implicating the replacement of an H atom on the ligand framework by an

O atom. Furthermore, **3** exhibits a resonance Raman spectrum (Figure S5) with vibrational features typical of an Fe^{III}–OAr chromophore.[14] This distinct switch in reactivity in the case of **2**-*syn* provides an unprecedented opportunity to monitor steps in the hydroxylation of an aromatic ring by a well-characterized Fe^{IV}=O species. Similar hydroxylations of phenyl rings attached to ligand frameworks with heterocyclic donors have been documented previously,[11] but this result represents the first example for a complex with a tetraalkylcyclam framework.

A solution of 1 mM **2**-*syn* in MeCN has a half-life ($t_{1/2}$) of approximately 11 min when formed at 298 K, based on the disappearance of absorption at 950 nm (Figure 2, bottom panel), a wavelength chosen to minimize interference from the growth of the broad and more intense band at 618 nm arising from the Fe^{III}–OAr product. An apparent "isosbestic point" can be observed at 830 nm that appears to indicate the clean transformation of **2**-*syn* to **3**.

Kinetic analysis shows that both the decay of **2**-*syn* (as monitored by the decrease in absorbance at 950 nm) and the generation of **3** (as followed by the increase in absorbance at 618 nm) can be fit by exponential functions with comparable first order rate constants of $1.3(1) \times 10^{-3}$ and $1.2(1) \times 10^{-3} \text{ s}^{-1}$, respectively (Figures 2, bottom panel, and S6). These observations support the notion that the decay of **2**-*syn* leads to the formation of the 618 nm chromophore, making it the rate-determining step (**rds**). Both the reaction rate and the yield of **3** (approx. 50%, estimated from Figure S7) are found to be insensitive to O_2, so O_2 does not play a role.

We have also deuterated the phenyl group of **1** to perturb its hydroxylation by the Fe^{IV}=O unit. Treatment of $Fe^{II}(Bn3MC-d_5)^{2+}$ (**1**-d_5, Figures S8 and S9) with 1.1 equiv *s*-ArIO at 298 K affords the the same near-IR band at 826 nm as observed for **2**-*syn*. The self-decay kinetics of **2**-*syn*-d_5 has almost the same reaction profile as its unlabeled counterpart, with the same rate constants for **2**-*syn* decay and **3** formation (Figure S10). Thus, the inverse KIE typically expected for an electrophilic aromatic substitution reaction is not observed.[2-b,10a] In fact, no KIE is found for either the decay of **2**-syn-d_5 or the generation of **3**-d_4, even though ESI-MS confirms the loss of a deuterium atom upon ring hydroxylation (Figure S8), suggesting that aromatic C–H bond cleavage must not be involved in the rate-determining step of the reaction.

However, there are subtle differences in the kinetic behavior of the two isotopomers, which are clarified when plots for the generation of **3** and **3**-d_4 are compared (Figure 3). Closer scrutiny of the 4000 s profile for the formation of **3** shows the presence of an initial lag phase (**LP**) in the first 35 seconds, after which the reaction exhibits a proper exponential growth behavior typical for a first-order reaction for the 618 nm chromophore (Figure 3, left panel, red box). The latter step, assigned to the formation of **3**, has a first order rate constant that matches that for the decay of **2**-*syn* (Figure 2, bottom panel inset). Interestingly, this **LP** becomes more pronounced upon deuteration of the phenyl group, doubling in length from approximately 35 to 70 s (the length of the **LP** being defined by the crossing point with the time axis of a linear extrapolation of the initial exponential growth; Figure 3, right panel). In contrast, such a lag phase is not
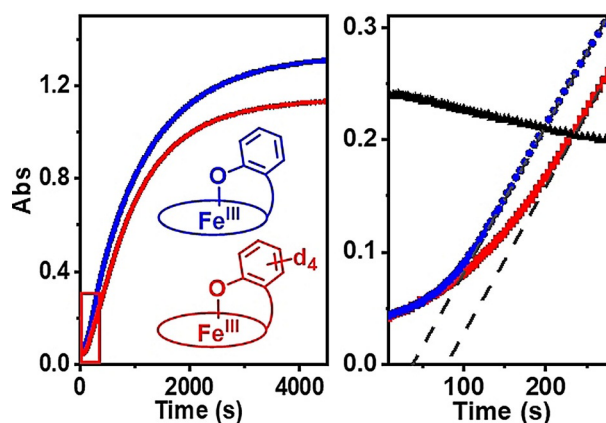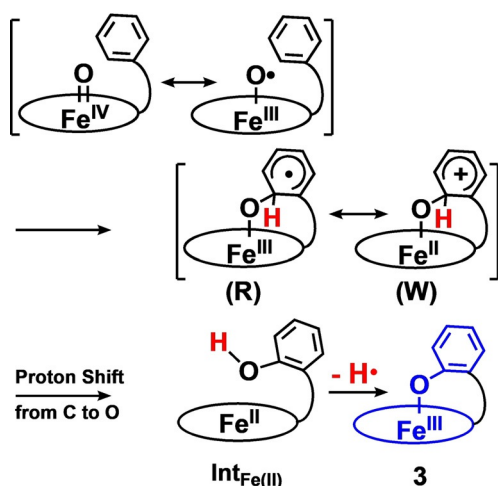

Figure 3. Left panel: Time traces at 618 nm reflecting the generation of **3** (blue line) and **3**-d_4 (red line) at 298 K. The red box is the region that is enlarged in the right panel. Right panel: Enlarged 0–300 s region showing the difference between the lag phases for **3** and **3**-d_4. The dashed lines represent linear extrapolations from the exponential curves in the accumulation of **3** (blue line) and **3**-d_4 (red line) to earlier time points, which cross the time axis, respectively at 35 and 70 s. The black line shows the absence of a lag phase in the decay of **2**-*syn*, as monitored at 950 nm within the same time window.

observed in the decay profile of **2**-*syn* (Figure 3, right panel, black trace), suggesting that the lag phase is not connected with the decay of **2**-*syn* but associated only with the generation of **3**. The existence of this lag phase and its enhancement upon deuteration of the phenyl ring suggest that there could be an intervening step involving an as yet unidentified intermediate between **2**-*syn* and **3**.

We have tracked the flow of electrons in as much detail as possible to find support for the involvement of an intermediate between **2**-*syn* and **3**. From a scrutiny of their structures, it is obvious that **2**-*syn* must lose an H atom in order to generate **3**. The ability of an Fe^{IV}=O species to carry out 1 e$^-$ oxidations may be facilitated by its acquisition of some Fe^{III}–oxyl character along the reaction trajectory (Scheme 3). Indeed, DFT calculations reveal the Fe^{III}–oxyl electromer to be one of its lower-lying excited states.[15] The hydroxylation of the phenyl group by an Fe^{IV}=O moiety can thus be considered as initiated by oxyl radical attack on the π system of the arene, avoiding the cleavage of its very strong aromatic C–H bond (approx. 110 kcal mol^{-1}). Such a step should result in the formation of a C–O bond that allows the unpaired electron to become delocalized onto the pentadienyl moiety (Scheme 3, intermediate **R**). Transfer of another electron from the pentadienyl radical moiety to the Fe^{III} center generates a Wheland intermediate bound to an Fe^{II} center (Scheme 3, intermediate **W**), which is predicted by a computational study to be thermodynamically more stable than intermediate **R**.[10a] Subsequent aromatization of **W** is accomplished by a proton shift from the *ipso*-C atom to the O atom of the nascent phenolate, which is the only basic site in the system, to form an Fe^{II}–phenol species we designate as $\text{Int}_{Fe(II)}$ (Scheme 3). In the last step of the reaction, $\text{Int}_{Fe(II)}$ is in turn oxidized to the highly chromophoric **3** via the transfer of the H atom from the nascent hydroxy group of the pendant phenol of $\text{Int}_{Fe(II)}$ to residual **2**-*syn*.

20994 www.angewandte.org

© 2021 Wiley-VCH GmbH

Angew. Chem. Int. Ed. **2021**, *60*, 20991–20998

Scheme 3. A reactivity mode for aromatic substrates in which the Fe^{IV}=O moiety attacks a phenyl ring to form a C−O bond to generate a pentadienyl radical intermediate (**R**). Tautomerization of **R** yields an electromer in which the iron center is reduced to the Fe^{II} state with a bound Wheland intermediate (**W**). Subsequent conversion of **W** to **Int$_{Fe(II)}$** by a proton shift from C to O and followed by loss of an H atom generates **3**.

Mechanistic Analysis

The reaction mechanism proposed in Scheme 3 involves an initial intramolecular step with the Fe^{IV}=O unit of **2**-*syn* attacking the pendant phenyl ring to effect its hydroxylation and leading to **Int$_{Fe(II)}$**. This step is followed by the rapid transfer of an H atom on **Int$_{Fe(II)}$** to residual **2**-*syn* to form the highly chromophoric **3**. In the reaction mixture derived from the reaction of *s*-ArIO with **1**, **2**-*syn* and **2**-*anti* represent the only two potential oxidants present in solution at the start that are the likely acceptors for the H atom generated in the conversion of **2**-*syn* to **3**. As shown by NMR (Figure S11), **2**-*anti* remains unchanged throughout the reaction process. It thus behaves merely as a spectator species, leaving **2**-*syn* as the only oxidant available in the reaction.

In our proposed mechanism, **2**-*syn* must play two roles. Its primary role is the intramolecular hydroxylation of the phenyl ring to form **Int$_{Fe(II)}$**, and its secondary role is to extract an H atom from **Int$_{Fe(II)}$** in the conversion of the latter to **3**, which is a bimolecular reaction (Scheme 3). As a consequence, the generation of **3** should be affected by changing the concentration of **2**-*syn* as its formation is an intermolecular reaction, but the intramolecular generation of **Int$_{Fe(II)}$** should not. In addition, a fraction of **2**-*syn* must become reduced to balance the reaction and convert into an Fe^{III}−OH derivative or the Fe^{II}−OH$_2$ product **1**.

To answer the questions raised above, we have investigated the effect of changing the concentration of **2**-*syn*. At 0.7 mM **2**-*syn* decays at a rate of $1.3(1) \times 10^{-3}$ s^{-1} and **3** is generated at a rate of $1.2(1) \times 10^{-3}$ s^{-1} (Figure S10), values that are essentially the same as those for the 1 mM experiment (see Figure 2 bottom and accompanying text). However, when the **2**-*syn* concentration is further reduced to 0.3 mM, the two steps become more asynchronous. **2**-*syn* decays as soon as it is generated at a rate of about $1.4(1) \times 10^{-3}$ s^{-1},

which is comparable to values obtained at the other two concentrations of **2**-*syn* (Figure 4 A, gray traces and Figure S10), but the generation of **3** slows to $1.0(1) \times 10^{-3}$ s^{-1}, a rate constant distinct from that for the decay of **2**-*syn* (Figure 4 A, blue traces and Figure S10). As a consequence, the crossing points of the traces progressively shift to the right as the reaction proceeds, resulting in the disappearance of the isosbestic point observed in the 1 mM experiment (Figure 4 A, inset vs. Figure 2, bottom). Unlike at higher concentrations of **2**-*syn*, the decay of **2**-*syn* is no longer clearly the rate-determining step and the formation of **3** has become slow enough to become competitive with **2**-*syn* decay. Figure 4 B compares the growth curves of the 618 nm chromophore obtained from 0.3, 0.7, and 1.0 mM solutions of **2**-*syn*. All are plotted with normalized absorbance to allow a visual comparison of their **LP**s together with a first-order curve through the zero point (Figure 4 B, red dashed trace). The decrease in the concentration of **2**-*syn* results in growth curves of the corresponding 618-nm band that progressively deviate from
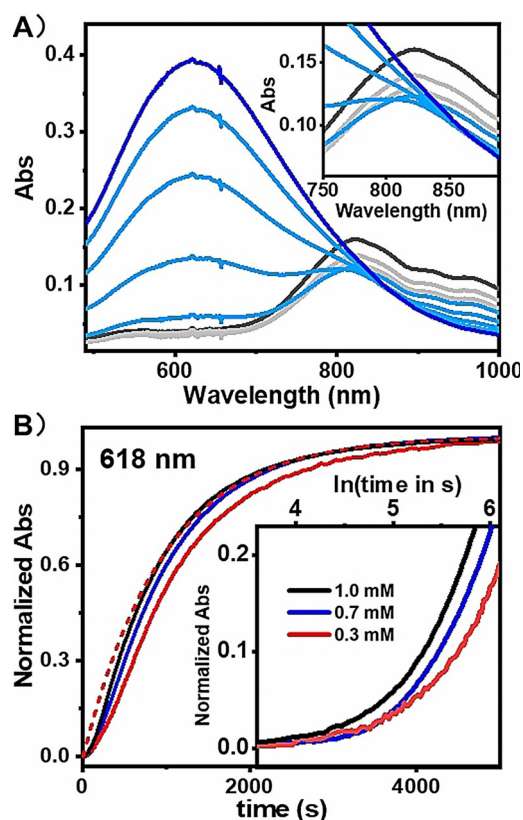

Figure 4. A) Conversion of 0.3 mM **2**-*syn* in MeCN (black trace) to **3** (blue trace) at 298 K over a 90 min period. Gray and lighter blue traces correspond, respectively, to the decay of **2**-*syn* and the growth of **3** during the conversion. Inset shows the enlarged 750–900 nm region, emphasizing the asynchrony of the two steps. B) Comparison of time traces at 618 nm associated with the generation of **3** from initial concentrations of **2**-*syn* of 1.0 mM (black), 0.7 mM (blue), and 0.3 mM (red). Curves have been normalized to facilitate visual comparison. The dashed red line represents ideal exponential behavior. Note the more pronounced initial lag phase observed for the 0.3 mM sample. Inset shows plots of the initial 500 seconds versus ln(time) to highlight the lengthening lag phase at the onset of the reaction with decreasing [**2**-*syn*].

the standard exponential curve. In particular, the curve shape for the 0.3 mm experiment (Figure 4B, red solid trace) does not overlap at all with the standard, further supporting the notion that the decay of **2**-*syn* has become faster than the generation of **3** in this case. Inset shows plots of the initial 500 seconds versus time in logarithmic scale to highlight the lengthening of the **LP**s at the onset of the reaction with decreasing **2**-*syn* concentration.

These observations agree with our analysis of the reaction scheme: the reaction leading to **3** is a bimolecular reaction that is affected by the concentration of **2**-*syn*. Due to its intermolecular nature, the generation of **3** is more sensitive to the decreasing concentration of **2**-*syn* than the intramolecular decay of **2**-*syn* such that the formation of **3** becomes obviously slower than the decay of **2**-*syn* in the experiment with 0.3 mm **2**-syn. This mechanistic hypothesis is corroborated by the lengthening of **LP** upon deuteration of the phenyl ring, reflecting the kinetic isotope effect (KIE) for the slower "D atom" transfer step from **2**-*syn*-d_5 (Figure 3). In conclusion, **3** is the product of **Int$_{Fe(II)}$** reacting with residual **2**-*syn*, in agreement with the observed kinetic data where the generation rate of **3** drops faster than the decay rate of **2**-*syn*, as both reactants leading to **3** have a first-order dependence on the concentration of **2**-*syn*.

We have also monitored the reaction by ^{1}H NMR to identify other components of the reaction mixture. Over the course of an hour, signals from **2**-*anti* remain unchanged in intensity relative to the residual 1-(*tert*-butylsulfonyl)-2-iodobenzene (*s*-ArI) byproduct from the *s*-ArIO internal standard (Figure 5, Figure S11). However, two sharp peaks at 11.3 and 13.5 ppm are observed to grow as the reaction progresses and can be assigned to H$_o$ and H$_m$ of **1** (Figure S12a); other NMR features of **1** can also be found upon the decay of **2**-*syn* (Figure S12b). Taken together, these data

show that **1** is in fact regenerated in approximately 30 % yield, which accounts for roughly 1/3 of the starting **2**-*syn* (approximately 80 %). Taking into consideration the approximately 50 % yield of the major product **3** and the approximately 30 % yield of **1**, it becomes clear that **2**-*syn* decay affords **3** and **1** in a 2:1 ratio, with the remaining approximately 20 % being **2**-*anti*, the typical side-product in the generation of **2**-*syn* with *s*-ArIO, which remains uninvolved in the reaction pathway (Figure S11).

With the spectroscopic results described above, we have tracked the fate of **2**-*syn* in its conversion into a 2:1 ratio of **3** and **1** products. There is no direct evidence found for the two species that bridge the gap between **2**-*syn* and its products. **Int$_{Fe(II)}$** is an isomer of **2**-*syn* that when formed is proposed to convert immediately to **3** by the loss of an H atom (Scheme 4). The H atom released is absorbed by residual **2**-*syn*, which is in turn reduced back to **1** and one equivalent of H$_2$O. Both the starting material and the product can be observed by NMR and quantified to establish the reaction stoichiometry summarized in Scheme 4.

The chemistry represented by the initial step in the model system in the conversion of **2**-*syn* to **Int$_{Fe(II)}$** corresponds to that for the key transformation catalyzed by the nonheme iron enzyme phenylalanine hydroxylase, in which an Fe^{IV}=O
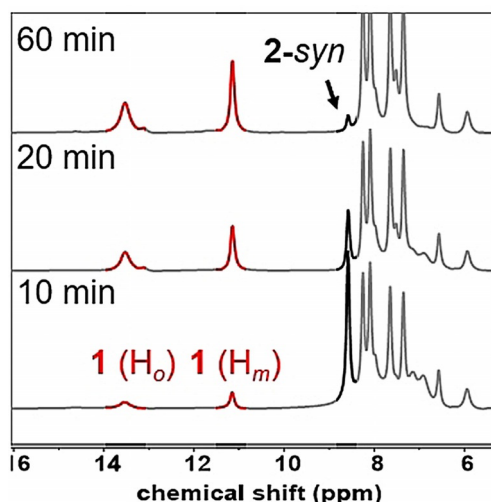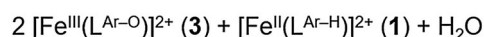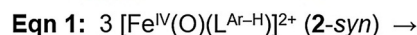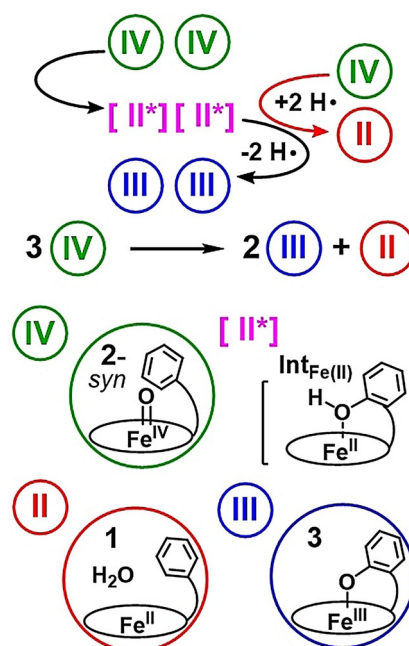

Figure 5. NMR spectra of the reaction taken 10, 20, and 60 min after mixing 10 mm **1** with 1.1 equiv *s*-ArIO at 298 K in MeCN-d_3. The sharp peak at 8.5 ppm is associated with phenyl protons on **2**-*syn*, which decreases in intensity upon conversion of **2**-*syn* to **3**. Concomitantly, the red-labeled peaks at 11.3 and 13.5 ppm assigned to the *ortho* and *meta* proton signals of the phenyl group of **1** grow in intensity during the course of the transformation.

Eqn 1: 3 [Fe^{IV}(O)(L^{Ar-H})]$^{2+}$ (**2**-*syn*) →

2 [Fe^{III}(L^{Ar-O})]$^{2+}$ (**3**) + [Fe^{II}(L^{Ar-H})]$^{2+}$ (**1**) + H$_2$O

Scheme 4. Top: Proposed mechanism for the aromatic hydroxylation reaction performed by the oxoiron(IV) species **2**-*syn*. The first step is the conversion of **2**-*syn* (or (IV)) into the unobserved **Int$_{Fe(II)}$** (or [II*]) by insertion of the oxo atom into the target C−H bond. In the next step, **Int$_{Fe(II)}$** is oxidized to **3** (or (III)) by transfer of an H atom to residual **2**-*syn*. Two consecutive H atom transfers to **2**-*syn* generate a molecule of **1** (or (II)). Overall, the reaction converts 3 equiv **2**-*syn* into 2 equiv **3** and 1 equiv **1**, for a theoretical yield of 67 % for **3** and 33 % for **1**. Bottom: Structures associated with the four species involved in the reaction.

20996 www.angewandte.org

© 2021 Wiley-VCH GmbH

Angew. Chem. Int. Ed. **2021**, *60*, 20991 – 20998

oxidant generated at the iron active site hydroxylates the phenylalanine substrate to form tyrosine. In the case of the enzyme, the tyrosine product is released from the active site, and the starting Fe^{II} center is regenerated for the next cycle of catalysis.[3a–e] However, for our biomimetic Bn3MC complex, the analogue to the enzyme–product complex is in fact **$Int_{Fe(II)}$**, but it rapidly reacts with residual $Fe^{IV}=O$ oxidant, which extracts the equivalent of an H atom from **$Int_{Fe(II)}$** to generate the blue-colored product **3** (Scheme 3), thereby preventing the initiation of the next cycle of oxidation. It would be impossible for this latter step to occur in the isolation of the enzyme active site.

Lastly, the formation of chromophoric **3** provides a spectroscopic handle with which to probe the relative energetics of intramolecular aromatic hydroxylation versus intermolecular aliphatic C−H bond cleavage by the nascent **2-*syn*** species. We find that the addition of even 1 equiv cyclohexadiene (CHD, $D_{C–H}$ 76 kcal mol^{-1}) to the reaction mixture results in the immediate interception of **2-*syn***, decreasing the yield of **3** to approximately 20 % (Figure S13). The yield of **3** drops even further to approximately 10 % with 5 equiv CHD. On the other hand, no noticeable interception is observed with 100 equiv toluene ($D_{C–H}$ 90 kcal mol^{-1}), thereby bracketing the strength of aliphatic C−H bonds that can be cleaved by **2-*syn***. The most intriguing result comes from using cyclohexene ($D_{C–H}$ 82 kcal mol^{-1}) as the intercepting substrate. Self-hydroxylation is predominantly observed in the presence of 10 equiv cyclohexene, but increasing to 100 equiv cyclohexene results in 80 % interception (Figure S14). The clear switch between competing reaction pathways in this series of cyclohexene experiments demonstrates the comparable activation barriers for the two reactions described, providing a qualitative understanding of the barriers for an oxoiron(IV) species to hydroxylate its pendant aromatic ring versus oxidizing an externally added substrate.

Conclusion

In the current study, we have demonstrated that the thermal decay of $[Fe^{IV}(O)(Bn3MC)]^{2+}$ (**2-*syn***) results in the hydroxylation of the pendant phenyl ring leading to the formation of $Fe^{III}−OAr$ (**3**) and $[Fe^{II}(Bn3MC)]^{2+}$ (**1**) products in a 2:1 ratio (Scheme 4). This study identifies for the first time the formation of the latter as a byproduct of the reaction, accounting completely for the electron flow and stoichiometry within this system. Thus, our proposed reaction scheme rationalizes the consistently observed 65 % yield of the $Fe^{III}−$OAr product reported for the three different $Fe^{IV}=O$ complexes that effect intramolecular arene hydroxylation.[11a,f] With the general problem identified in our example that the reaction between residual **2-*syn*** and **$Int_{Fe(II)}$** prevents a proper biomimetic catalytic cycle to be completed, measures could be taken to improve the design of the biomimetic system to minimize such side reactions.

Moreover, our results reveal that the $Fe^{IV}=O$ oxidant of a TMC-derived ligand is actually powerful enough to hydroxylate a pendant phenyl ring. This intramolecular hydroxylation is in fact competitive with the intermolecular hydroxylation of cyclohexene, qualitatively providing an experimental estimate of the activation barrier for such a reaction for the first time. Although previous DFT calculations by de Visser to assess the reactivity of $[Fe^{IV}(O)-(TMC)(NCMe)]^{2+}$ had revealed a strong preference for the hydroxylation for aliphatic C−H bonds over aromatic hydroxylation,[16] the experimental results reported here demonstrate that this $Fe^{IV}=O$ unit has a more versatile reactivity than predicted by these DFT calculations.

Conflict of Interest

The authors declare no conflict of interest.

[1] G. A. Olah, Á. Molnár, G. K. S. Prakash, *Hydrocarbon Chemistry, Vol. 1 & 2*, Wiley, Hoboken, **2018**.

[2] a) J. F. Bunnett, R. E. Zahler, *Chem. Rev.* **1951**, *49*, 273; b) F. A. Carey, R. J. Sundberg, *Advanced Organic Chemistry: Part B: Reactions and Synthesis* Springer US, Boston, **1983**, p. 375; c) H. Heaney in *Comprehensive Organic Synthesis* (Eds.: B. M. Trost, I. Fleming), Pergamon, Oxford, **1991**, p. 733; d) G. A. Olah, *Superacid Chemistry*, Wiley-Blackwell, Oxford, **2009**; e) V. Snieckus, *Beilstein J. Org. Chem.* **2011**, *7*, 1215.

[3] a) P. F. Fitzpatrick, *Biochemistry* **2003**, *42*, 14083; b) M. Costas, M. P. Mehn, M. P. Jensen, L. Que, *Chem. Rev.* **2004**, *104*, 939; c) P. C. A. Bruijnincx, G. van Koten, R. J. M. Klein Gebbink, *Chem. Soc. Rev.* **2008**, *37*, 2716; d) E. G. Kovaleva, J. D. Lipscomb, *Nat. Chem. Biol.* **2008**, *4*, 186; e) S. Kal, L. Que, *J. Biol. Inorg. Chem.* **2017**, *22*, 339.

[4] a) B. E. Eser, E. W. Barr, P. A. Frantom, L. Saleh, J. M. Bollinger, C. Krebs, P. F. Fitzpatrick, *J. Am. Chem. Soc.* **2007**, *129*, 11334; b) A. J. Panay, M. Lee, C. Krebs, J. M. Bollinger, P. F. Fitzpatrick, *Biochemistry* **2011**, *50*, 1928.

[5] J.-U. Rohde, J.-H. In, M. H. Lim, W. W. Brennessel, M. R. Bukowski, A. Stubna, E. Münck, W. Nam, L. Que, *Science* **2003**, *299*, 1037.

[6] a) A. R. McDonald, L. Que, *Coord. Chem. Rev.* **2013**, *257*, 414; b) M. Guo, T. Corona, K. Ray, W. Nam, *ACS Cent. Sci.* **2019**, *5*, 13; c) C. A. Abelson, A. M. Aboelenen, W. Rasheed, L. Que, Jr., *Chapter 8.17 – Synthetic Nonheme High-Valent Iron-Oxo Complexes: Structures and Oxidative Function*, In *Comprehensive Coordination Chemistry III: from Biology to Nanotechnology* (Eds. E. Constable, G. Parkin, L. Que, Jr.), Elsevier Ltd., **2021**, *8*, pp. 412 – 454.

[7] a) J. C. Price, E. W. Barr, T. E. Glass, C. Krebs, J. M. Bollinger, *J. Am. Chem. Soc.* **2003**, *125*, 13008; b) L. M. Hoffart, E. W. Barr, R. B. Guyer, J. M. Bollinger, C. Krebs, *Proc. Natl. Acad. Sci. USA* **2006**, *103*, 14738; c) D. Galonić Fujimori, E. W. Barr, M. L. Matthews, G. M. Koch, J. R. Yonce, C. T. Walsh, J. M. Bollinger, C. Krebs, P. J. Riggs-Gelasco, *J. Am. Chem. Soc.* **2007**, *129*, 13408; d) M. L. Matthews, C. M. Krest, E. W. Barr, F. H. Vaillancourt, C. T. Walsh, M. T. Green, C. Krebs, J. M. Bollinger, *Biochemistry* **2009**, *48*, 4331.

[8] a) K.-B. Cho, X. Wu, Y.-M. Lee, Y. H. Kwon, S. Shaik, W. Nam, *J. Am. Chem. Soc.* **2012**, *134*, 20222; b) K.-B. Cho, H. Hirao, S. Shaik, W. Nam, *Chem. Soc. Rev.* **2016**, *45*, 1197.

[9] a) A. N. Biswas, M. Puri, K. K. Meier, W. N. Oloo, G. T. Rohde, E. L. Bominaar, E. Münck, L. Que, *J. Am. Chem. Soc.* **2015**, *137*, 2428; b) S. H. Bae, M. S. Seo, Y.-M. Lee, K.-B. Cho, W.-S. Kim, W. Nam, *Angew. Chem. Int. Ed.* **2016**, *55*, 8027; *Angew. Chem.* **2016**, *128*, 8159; c) X. Engelmann, D. D. Malik, T. Corona, K. Warm, E. R. Farquhar, M. Swart, W. Nam, K. Ray, *Angew. Chem. Int. Ed.* **2019**, *58*, 4012; *Angew. Chem.* **2019**, *131*, 4052; d) J. P. Biswas, M. Ansari, A. Paik, S. Sasmal, S. Paul, S. Rana, G. Rajaraman, D. Maiti, *Angew. Chem. Int. Ed.* **2021**, *60*, 14030; *Angew. Chem.* **2021**, *133*, 14149.

[10] a) S. P. de Visser, K. Oh, A.-R. Han, W. Nam, *Inorg. Chem.* **2007**, *46*, 4632; b) J. P. Bigi, W. H. Harman, B. Lassalle-Kaiser, D. M. Robles, T. A. Stich, J. Yano, R. D. Britt, C. J. Chang, *J. Am. Chem. Soc.* **2012**, *134*, 1536; c) S. Sahu, M. G. Quesne, C. G. Davies, M. Durr, I. Ivanovic-Burmazovic, M. A. Siegler, G. N. Jameson, S. P. de Visser, D. P. Goldberg, *J. Am. Chem. Soc.* **2014**, *136*, 13542; d) S. Sahu, B. Zhang, C. J. Pollock, M. Durr, C. G. Davies, A. M. Confer, I. Ivanovic-Burmazovic, M. A. Siegler, G. N. Jameson, C. Krebs, D. P. Goldberg, *J. Am. Chem. Soc.* **2016**, *138*, 12791.

[11] a) S. Sahu, L. R. Widger, M. G. Quesne, S. P. de Visser, H. Matsumura, P. Moenne-Loccoz, M. A. Siegler, D. P. Goldberg, *J. Am. Chem. Soc.* **2013**, *135*, 10590; b) G. de Ruiter, N. B. Thompson, M. K. Takase, T. Agapie, *J. Am. Chem. Soc.* **2016**, *138*, 1486; c) E. L. Hegg, R. Y. N. Ho, L. Que, *J. Am. Chem. Soc.* **1999**, *121*, 1972; d) S. J. Lange, H. Miyake, L. Que, *J. Am. Chem. Soc.* **1999**, *121*, 6330; e) Y. Mekmouche, S. Ménage, C. Toia-Duboc, M. Fontecave, J.-B. Galey, C. Lebrun, J. Pécaut, *Angew. Chem. Int. Ed.* **2001**, *40*, 949; *Angew. Chem.* **2001**, *113*, 975; f) M. P. Jensen, S. J. Lange, M. P. Mehn, E. L. Que, L. Que, *J. Am. Chem. Soc.* **2003**, *125*, 2113; g) M. P. Jensen, M. P. Mehn, L. Que, Jr., *Angew. Chem. Int. Ed.* **2003**, *42*, 4357; *Angew. Chem.* **2003**, *115*, 4493; h) M. P. Mehn, K. Fujisawa, E. L. Hegg, L. Que, *J. Am. Chem. Soc.* **2003**, *125*, 7828; i) A. Nielsen, F. B. Larsen, A. D. Bond, C. J. McKenzie, *Angew. Chem. Int. Ed.* **2006**, *45*, 1602; *Angew. Chem.* **2006**, *118*, 1632; j) W. H. Harman, C. J. Chang, *J. Am. Chem. Soc.* **2007**, *129*, 15128.

[12] J. Prakash, G. T. Rohde, K. K. Meier, E. Münck, L. Que, *Inorg. Chem.* **2015**, *54*, 11055.

[13] J. Prakash, Y. Sheng, A. Draksharapu, J. E. M. N. Klein, C. J. Cramer, L. Que, Jr., *Angew. Chem. Int. Ed.* **2019**, *58*, 1995; *Angew. Chem.* **2019**, *131*, 2017.

[14] L. Que, Jr., *Coord. Chem. Rev.* **1983**, *50*, 73.

[15] a) S. Ye, F. Neese, *Curr. Opin. Chem. Biol.* **2009**, *13*, 89; b) S. Ye, F. Neese, *Proc. Natl. Acad. Sci. USA* **2011**, *108*, 1228; c) B. K. Mai, Y. Kim, *Inorg. Chem.* **2016**, *55*, 3844.

[16] S. P. de Visser, R. Latifi, L. Tahsini, W. Nam, *Chem. Asian J.* **2011**, *6*, 493.

20998   www.angewandte.org

© 2021 Wiley-VCH GmbH

Angew. Chem. Int. Ed. **2021**, *60*, 20991 – 20998